Overlap of the plasmasphere and ring current: Relation to subauroral ionospheric heating

C. Gurgiolo,[1] B. R. Sandel,[2] J. D. Perez,[3] D. G. Mitchell,[4] C. J. Pollock,[5] and B. A. Larsen[6]

Received 20 December 2004; revised 30 August 2005; accepted 5 October 2005; published 16 December 2005.

[1] The overlap of the ring current with the outer plasmasphere is thought to play a major role in storm-time related increases in the subauroral ambient topside electron temperature. Instabilities generated within the overlap region, Coulomb collisions of plasmaspheric electrons with the ring current ions, and charge exchange are all thought to work either individually or together to generate a downward heat flux into the ionosphere to produce the increase in temperature. Analysis of IMAGE two-dimensional ring current and plasmasphere density maps together with in situ DMSP ambient electron temperature data shows that the heating generally occurs over a small radial extent within the plasmasphere/ring current overlap region and may be significantly earthward of the plasmapause. This argues against collisional heat conduction as the source of the heat flux and for an instability-based process. The finding that the heating occurs within well-defined ratios of the cold plasmasphere to hot ring current density strengthens this supposition.

Citation: Gurgiolo, C., B. R. Sandel, J. D. Perez, D. G. Mitchell, C. J. Pollock, and B. A. Larsen (2005), Overlap of the plasmasphere and ring current: Relation to subauroral ionospheric heating, *J. Geophys. Res.*, *110*, A12217, doi:10.1029/2004JA010986.

1. Introduction

[2] Enhancements in the topside ambient subauroral electrons temperature are an ubiquitous feature during storm-time conditions and are thought to be a consequence of a downward heat flux generated within the overlap of the ring current and plasmasphere. The region includes not only the plasmasphere boundary layer (PBL) as defined by *Carpenter and Lemaire* [2004] but also what most would consider the plasmasphere proper. The heating more than likely originates in the decay of the ring current [*Fok et al.*, 1991] and has been the focus of numerous papers and looked at from multiple perspectives. The close relationship of regions of enhanced heating to the plasmapause has been addressed by many authors [e.g., see *Green et al.*, 1986; *Brace et al.*, 1988]. *Brace et al.* [1988] have further noted that the heating in the dusk sector appears to occur at the position of the inner plasmapause where there is a larger density gradient rather than at the outer edge of the duskside plasmaspheric bulge.

[3] The subauroral enhancement in the ionospheric heating is the energy source which drives Stable Auroral Red (SAR) arc [*Norton and Findley*, 1969; *Chandra et al.*, 1972] and much of the work in identifying sources of the heat flux has been driven by SAR arc studies. It should be pointed out, however, that while the heating forms a necessary condition for SAR arc generation it is not a sufficient condition in itself [*Kozyra et al.*, 1982]. Conjugate satellite and ground observations show that SAR arcs rarely exists over the entire region of the thermal enhancement but are generally localized within an electron trough [*Foster et al.*, 1994] where the heating is increased due to the lower local density and more likely to reach the threshold necessary for the excitation of the emission.

[4] Multiple mechanisms have been proposed to drive the heat flux responsible for the anomalous increases in the ionospheric electron temperature. All are based on a ring current interaction with the plasmasphere and are generally benchmarked against their potential to raise the ionospheric electron temperature above the threshold necessary to produce a SAR arc. A brief survey of the mechanisms and their effectiveness can be found in the work of *Khazanov et al.* [1992].

[5] *Cole* [1965, 1975] used Coulomb collisions of the plasmaspheric electrons with the ring current H^+ ions to produce a heated plasmaspheric electron population with collisional heat conductance used to establish the downward heat flux. *Kozyra et al.* [1987] extended this to include Coulomb collisions between the plasmaspheric electrons and energetic ring current O^+ ions but left the method of heat transfer open. Measurements of magnetospheric conditions during several observed SAR arcs showed that Coulomb collisions could produce the necessary heating to drive the emissions. *Fok et al.* [1993] in a two-dimensional simulation study of ring current decay presented a global

[1]Bitterroot Basic Research, Hamilton, Montana, USA.
[2]Lunar and Planetary Laboratory, University of Arizona, Tucson, Arizona, USA.
[3]Physics Department, Auburn University, Auburn, Alabama, USA.
[4]John Hopkins University Applied Physics Laboratory, Laurel, Maryland, USA.
[5]Southwest Research Institute, San Antonio, Texas, USA.
[6]Department of Physics, Montana State University, Bozeman, Montana, USA.

0148-0227/05/2004JA010986

picture of the heating produced by Coulomb collisions concluding that even in the dawn sector sufficient heat flux would be generated for SAR arc production.

[6] *Cornwall et al.* [1971] suggested heating the plasmaspheric electrons through resonant Landau damping of H^+ generated ion cyclotron waves. *Thorne and Horne* [1997] extended this to include O^+ generated ion cyclotron waves. Direct scattering of the electrons into the loss cone coupled with conduction by collisionless strong diffusion provides the mechanism to transport the heat into the upper ionosphere. Under nominal conditions, heating by ion cyclotron waves was shown to be able to supply sufficient heat to drive a typical SAR arc. Using measured ring current and plasmasphere particle distributions in conjunction with a hydromagnetic model, both *Gorbachev et al.* [1992] and *Khazanov et al.* [1994] have derived ionospheric electron and ion temperature profiles expected from the generation of equatorial ion cyclotron waves which match well with measured profiles. Evidence of ion cyclotron waves in association with ionospheric heating events have been reported by *Lundblad and Søraas* [1978] and *Erlandson et al.* [1993]. Both *Jordanova et al.* [2001] and *Khazanov et al.* [2003] have included the generation of ion cyclotron waves in two-dimensional ring current models. Simulations using actual storm time inputs show a strong growth in the ion cyclotron waves in the postnoon and premidnight sectors at the start of the main phase with gradual extension into the noon and midnight sectors as the storm progresses.

[7] *Hasagawa and Mima* [1978] proposed the possibility of in situ heating by kinetic Alfvén waves. Unlike either Coulomb collisions or ion cyclotron waves, the heating is accomplished by direct acceleration of the plasmaspheric electrons into the ionosphere by the parallel electric field associated with the wave. *Lanzerotti et al.* [1978] have reported the presence of kinetic Alfvén waves in conjunction with SAR arcs.

[8] There is no reason to opt for one mechanism over another. Undoubtedly, under the proper conditions each plays a part in the coupling of the ring current to the ionosphere either alone or in concert with the others. The goal is to understand when a mechanism might be expected to be active and what its role in the coupling is.

[9] One of the outstanding deficiencies in the study of the coupling of the ring current to the ionosphere is the lack of concurrent and conjugate magnetospheric and ionospheric plasma measurements over complete anomalous heating events. With few exceptions most investigations are based on one set of measurements with nominal values and positions for the remaining sets. As we show here, the assumption made by many that the observed ionospheric heating occurs at the plasmapause is not always correct.

[10] This paper presents a global view of the plasmasphere–ring current system during the 18–19 June 2001 (days 169–170) storm. This was a small storm having a well-defined onset and long recovery phase. We combine data from the IMAGE and DMSP satellites to have concurrent and conjugate plasma measurements from the plasmasphere, ring current, and topside ionosphere. IMAGE is used to provide two-dimensional (2-D) mappings of the plasma conditions in the geomagnetic equatorial plane out to 8 R_E for the ring current ions and out to 6 R_E for the plasmaspheric He^+ ions while DMSP provides in situ measurements of the ionospheric conditions at 800 km in both the dusk and dawn sectors. Data from the three DMSP satellites (F12, F13, F15) provide over 100 crossings of the plasmasphere during the times when the IMAGE spacecraft is at an altitude giving full coverage of the geomagnetic equatorial plane. Plots of the equatorial ion flux and plasmaspheric He^+ density along the DMSP orbit tracks allow direct comparison of the states of the three overlapping plasma populations along the satellite track. This is the first time conditions across entire subauroral heating events have been studied with supporting conjugate magnetospheric observations. The long-term goal of this work, of which this is but the first step, is to be able to use the global ion and plasmasphere density maps as a proxy to the global ionospheric heating.

2. Data

[11] We use data from multiple experiments on board the IMAGE and DMSP F-12, F-13, and F-15, satellites. Data from the IMAGE spacecraft provide 2-D coverage of the ring current and plasmasphere in the geomagnetic equatorial plane, while DMSP provides in situ monitoring of the ionospheric conditions including the ambient electron density and temperature and the energetic precipitating electron and ion fluxes.

[12] IMAGE was launched in March 2000 into an elliptical orbit of 0.15×7.2 R_E with a 14.2-hour orbital period. The spacecraft has a 2-min spin period that sets the temporal resolution of most measurements. The highly elliptical orbit provides long stretches of time with favorable observing geometry, that is, with lines of sight nearly perpendicular to the plane of the geomagnetic equator. This study makes extensive use of three IMAGE data sets.

[13] The Extreme Ultraviolet Imager (EUV) [*Sandel et al.*, 2000] measures the brightness of the He^+ 30.4-nm emission from the plasmasphere with a spatial resolution of 0.6 degrees (about 0.1 R_E) and a time resolution of 5 spins of the satellite (about 10 min). The measured brightness is directly proportional to the column abundance of He^+ along the lines of sight corresponding to each pixel. For this work, we invert the images of He^+ column abundance to maps of He^+ density in the plane of the geomagnetic equator. We describe the inversion method that we have developed especially for this purpose in the next section.

[14] Both the High and Medium Energy Neutral Atom imagers (HENA and MENA) return images of neutral atom fluxes. HENA [*Mitchell et al.*, 2000] operates in the 10–500 keV/nucleon range while MENA [*Pollock et al.*, 2000] operates in the 1 to 70 keV/nucleon range. Both experiments resolve both energy and mass. Inversions of the neutral atom images (NAI) provide global 2-D distributions of the ion flux in the geomagnetic equatorial plane. The basic inversion methods are covered by *Roelof and Skinner* [2000] and *Perez et al.* [2000] and are not discussed in the paper. To synchronize the NAI and the EUV inverted data, the NAIs are integrated for five spins prior to inversion. This has an added bonus of increasing the statistical accuracy in the NAIs.

[15] The DMSP satellites all follow circular polar orbits with a nominal altitude of 830 km and an orbital

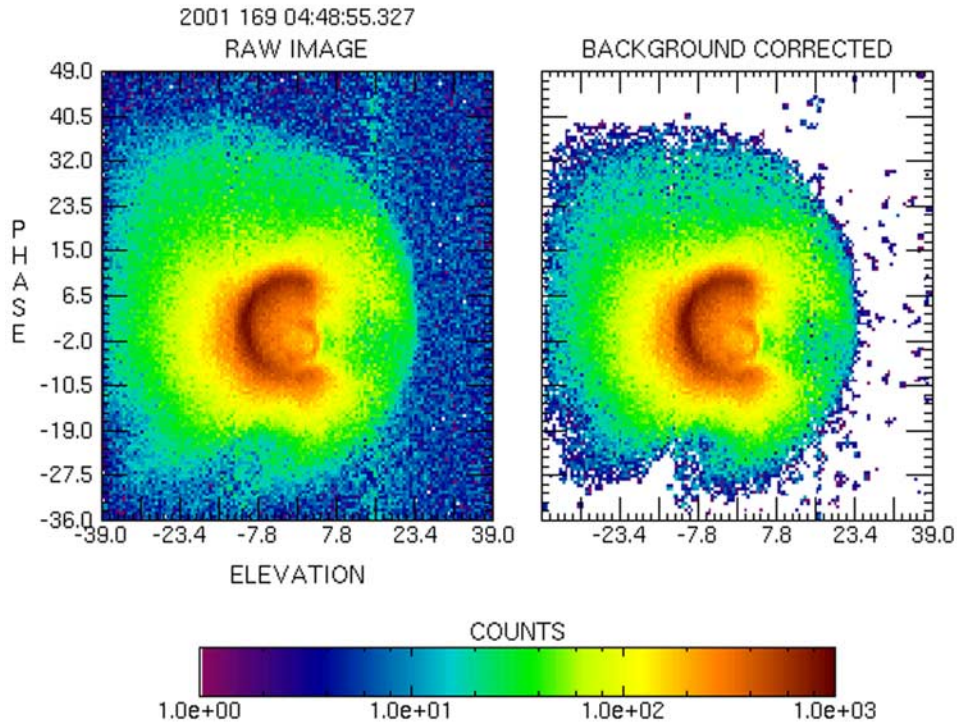

Figure 1. Measured EUV image (left) and the noise and background subtracted image (right).

period of 101 min. Orbits are approximately 0930–2120 LT (F-12, F-15) and approximately 1730–0530 LT (F-13). The satellites carry identical complements of instruments.

[16] The DMSP Special Sensor for Ions and Electrons (SSIES) experiment is a set of three sensors which include an ion drift meter (IDM), a retarding potential analyzer (RPA), and a Langmuir probe. Reduction of the SSIES data provides the ion density, temperature, and drift and the electron temperature along the satellite track. Measurements are provided on 4 s centers.

[17] The DMSP SSJ/4 experiment is a set of four sensors, two measuring the precipitating electrons and two measuring the precipitating ions along the satellite track. The total energy range covered for both species is 30 eV to 30 keV in 20 energy channels, 10 per sensor. Each pair of sensors has one common overlapping energy channel leaving 19 distinct energy bands per species. We use these measurements mainly to establish the equatorward boundary of the auroral zone.

3. Inversion of the EUV Images

[18] As the technique to invert EUV images to produce a global mapping of the He^+ density is new, we include a detailed description of it. An EUV image is a two-dimensional representation of the three-dimensional plasmaspheric He^+ density profile. Under the assumption that the He^+ density is constant along L, the images can be inverted to produce two-dimensional density maps of the He^+ ion population in the geomagnetic equatorial plane. The field is assumed to be dipolar throughout the inversion region. This is not a significant compromise. Within the event studies the plasmasphere lies within an L of 4 during active periods and within an L of 5 during quiet periods. The inversion steps are outlined below.

[19] The reduction of background and noise in the measured image is paramount in the inversion. Background increases the error in the absolute density estimate

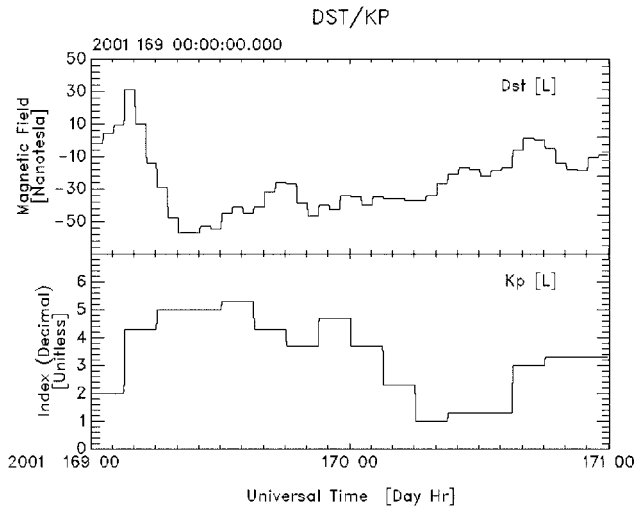

Figure 2. *Dst* and *Kp* indices across the time of the storm. Sudden commencement occurs close to 0400 UT on day 169.

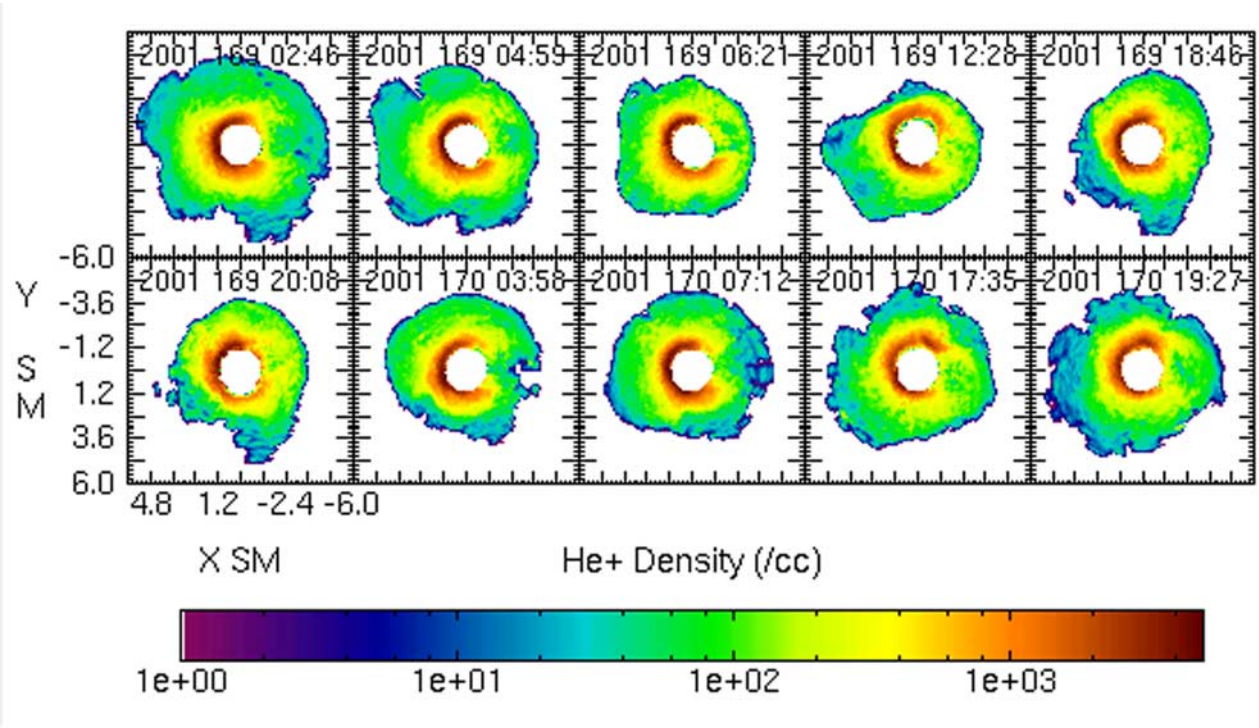

Figure 3. Inversions of selected EUV images across the storm time period. In each image the sun is to the left, dawn is up, dusk is down, and midnight is to the left. Plots depict the He^{+} ion density in the geomagnetic equatorial plane.

and noise is a major source of instability in the inversion. Removing the background and noise is a two-step process. First, the instrument background is removed by computing the average count rate in each column of the image for a fixed rotation angle above and below the area of interest and subtracting this average from each pixel in the column. The resultant image is then passed through a despeckling algorithm. This removes active and isolated pixel clusters. The cluster size is nominally set to two pixels. Figure 1 shows the results of a typical background and noise removal. The figure on the left is the original EUV image cropped to show just the plasmasphere region. The figure on the right is the background and noise subtracted image. The inversion begins with the cleaned image.

[20] The inversion uses an iterative approach in which an initial guess is modified repeatedly until it converges to a stable solution. The initial step in the iteration is the

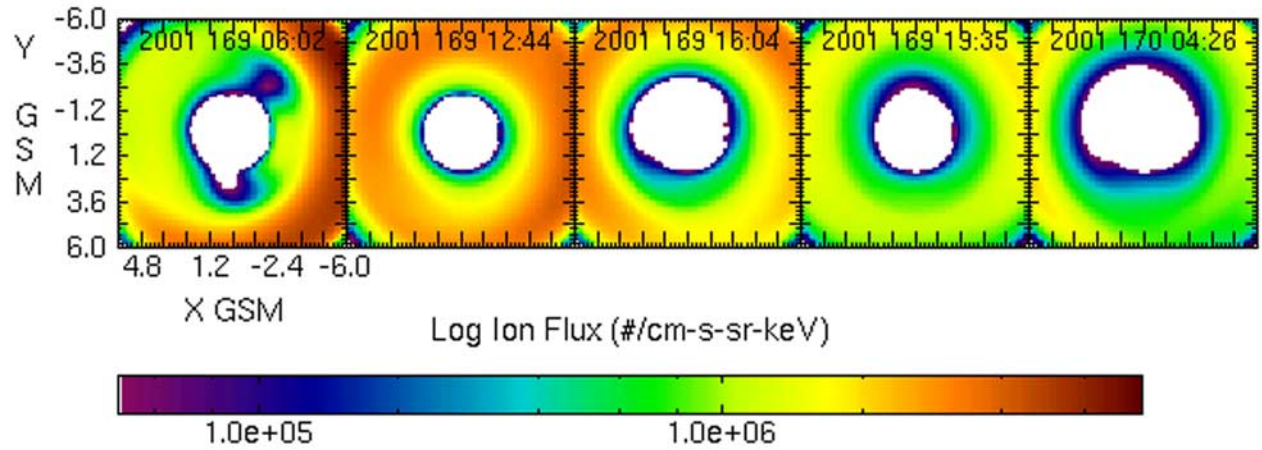

Figure 4. Selected inversions of the MENA 5.1–12.0 keV neutral images across the storm time. Plots depict ion flux in the geomagnetic equatorial plane.

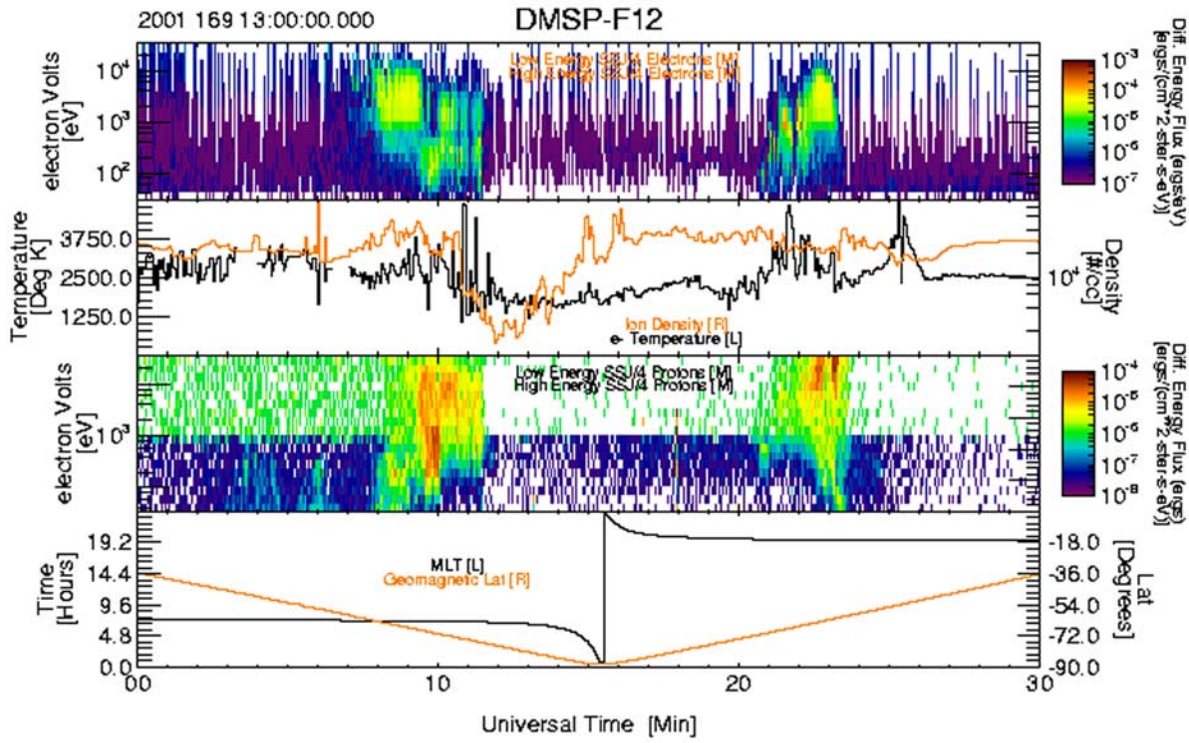

Figure 5. DMSP data showing a complete dawn to dusk southern hemisphere pass of F12. Top spectrogram shows precipitating electrons, and middle spectrogram shows precipitating ions. Both data sets are plotted in units of differential energy flux. Upper set of line plots shows the ambient electron temperature (black) and the ion density (orange). Lower set of line plots shows the satellite magnetic local time (black) and geomagnetic latitude (orange). An enhancement in the subauroral electron temperature is centered on 1325 UT.

formation of the zero solution and density matrices. Both matrices have identical order and represent a griding of the geomagnetic equatorial plane in L shell (L) $\times$ geomagnetic longitude (Λ) space. Both are overdimensioned to give them a higher spatial resolution than the EUV measurements. This is necessary both for stability and smoothness in the final solution.

[21] The density profile matrix holds the current density He^+ profile. The profile is initialized to a simple power law in L with no Λ dependence as

$$D = 10^{-.715L}.$$

The zero solution matrix holds a status flag for each grid in the density matrix. This flag is either zero or one, depending on whether the density of the grid is known to be zero or not. The matrix is initialized to all ones. Each EUV line of sight known to have a zero intensity is then mapped onto the zero solution matrix, and those grids it passes through are set to zero. Since the instrument measures column density, any pixel contained in a line of sight which has a zero total intensity associated with it must itself have zero density.

[22] Also set up in the initialization are the variable grids in the density matrix. These are the grids that are modified in each step in the iteration process and from which the new density matrix is built in each iteration step. There is one variable grid representing each instrument line of sight. This keeps the problem from being overconstrained in the iteration phase of the inversion. The variable grids form a unique set of unknowns and are set to the grids containing the closest approach to the Earth of each line of sight.

[23] Each iteration step begins with the construction of a synthetic image from the current density profile matrix. This is done in three steps. First, the zero solution matrix is used to mask off the zero intensity grids in the density matrix. Second, the column abundance along each of the instrument lines of sight is then computed from the modified density matrix. Any line of sight that is found to have only a single nonzero density value along it is set to zero and the zero solution matrix is updated. Lines of sight which have only a single nonzero value are generally noise which was not caught in the initial noise and background removal. Last, the column densities are modified by the instrument characteristics and the synthetic image is produced.

[24] The mean square deviation between the synthetic and measured image is then computed and compared to mean square deviations computed in previous iteration steps to see if a convergence has been reached. If so, the iterations are terminated and the current density profile is returned.

[25] When convergence has not been obtained, the measured image is divided by the synthetic image to produce a correction value for each line of sight. The density matrix is rebuilt using only the variable grid values multiplied by their corresponding correction value. All unassigned grids in the density profile matrix are filled using a 2-D linear

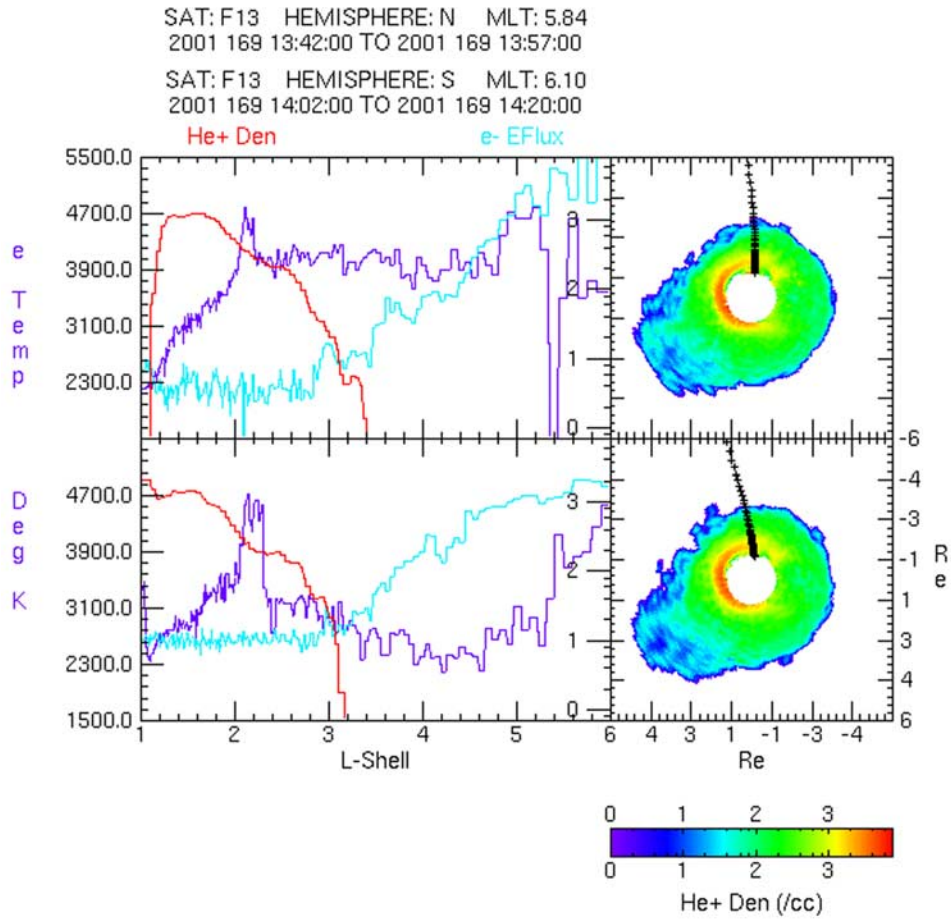

Figure 6. Consecutive north/south dusk sector crossings of the plasmasphere. Southern hemisphere portion of the crossing is covered in upper plots and the northern hemisphere portion of the crossing is covered in the lower plots. Traces in the left-hand plots are the plasmasphere He^+ density (red), the ionospheric temperature (blue), and the precipitating electron flux between 1 and 14 keV (cyan) along the satellite track. The scale for the plasmaspheric density trace is given along the right-hand axis. The electron flux trace has units of erg/cm^2 − s and is plotted against a logarithmic scale from 10^{-1} to 10^{-5} which is not explicitly shown in the plots. The right-hand plots show the equatorial projection of the plasmaspheric He^+ density at the time of the temperature enhancement overlaid by the satellite track. General information describing the plots is given in the two top labels (uppermost label goes with the top pair of plots). This information includes the beginning and ending time of the orbit track, the satellite from which the data was taken, the hemisphere in which the data was taken (north or south), and the magnetic local time (MLT) at a point midway through the time period. Both heating events are inner events; well earthward of the plasmapause ($\sim L = 3$) and reasonably narrow in extent. The events are conjugate.

least square fit algorithm. Last, the zero solution mask is applied to give the new density profile and a hot spot check is made. This is a search through the matrix for pixels which have intensities larger than their neighbors by some preset value. Such pixels represent solution which are either currently or in the process of becoming unstable. Their density is adjusted to the average value of their nearest neighbors. This concludes the iteration step which restarts with the computation of a new synthetic image.

[26] It should be noted that the inversion makes no special provision for either the dayglow contamination in the near-Earth sunlit portion of the EUV images or the dimmer plasmasphere seen within the Earth's shadow. Both are treated in the inversion as real phenomena. This results in an anomalous density enhancement in the sunlit sectors and a density depression directly antisunward of the Earth. The features are visible in all inversions.

4. Analysis

[27] Figure 2 shows the *Dst* and *Kp* indices over the 2 days of the storm. The storm begins with the sudden commencement which occurs between 0300 and 0400 UT on day 169. The main phase lasts for 6 to 8 hours, with a minimum depression in *Dst* of about −58 nT occurring

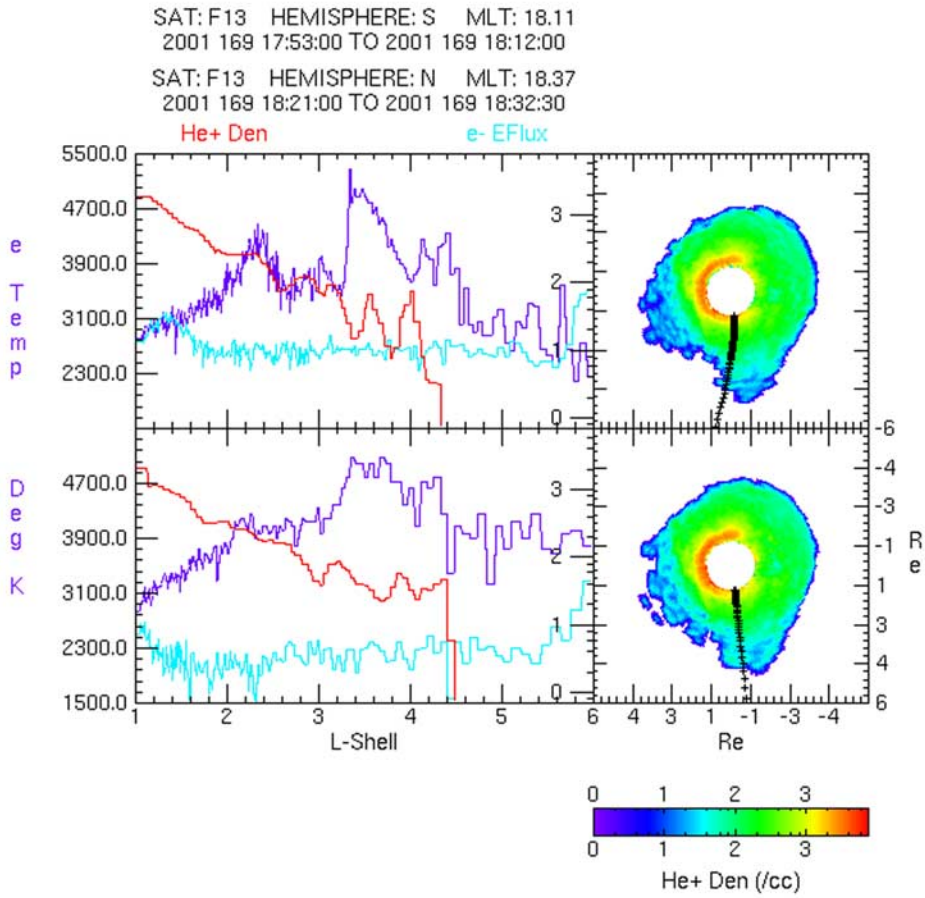

Figure 7. Identical to Figure 6 but for dusk sector crossing with the northern hemisphere portion of the pass depicted in the upper set of plots and the southern hemisphere portion in the lower set. Upper panel shows both an inner and outer heating event. In the lower panel the inner event is suppressed but discernible. Both events are conjugate. The outer events both occur within the PBL.

between 0800 and 1000 UT. *Kp* averages about 5 during this time. From hour 12 until the end of day 170 there is a slow recovery, with *Kp* gradually falling to its preevent level. At 1500 UT on day 170, *Kp* jumps to 3+ and remains there until the end of the plot.

[28] Figure 3 contains a selected set of 10 mappings of the global He^+ density covering the time period in Figure 1. Time runs left to right and top to bottom. Each plot is a 6 × 6 R_E Earth-centered cut through the geomagnetic equatorial plane. The white-centered region is the Earth which is not included in the inversion. The narrow, bright region seen on the sunlit side of the Earth is airglow contamination, while the depression in the density seen just antisunward of the Earth is due to the Earth's shadow.

[29] The first plot in the figure shows the plasmasphere prior to the onset of the storm (between 0256 and 0306 UT). The storm onset time was established from a significant jump in the EUV background in the image taken during this time period (and continuing into the next image) that results from the arrival of the high-energy solar protons at the storm onset. The plot depicts the local quiet-time plasmasphere for this event with the plasmasphere extending out to about 5 R_E. The next image, taken 2 hours after the storm onset, shows the beginning of erosion of the plasmasphere. By the third image, at which time the storm has entered the main phase, the plasmasphere has reached its minimum extent of about 3.5 R_E. For the next 20 or so hours the plasmasphere stays in this minimal or disturbed state and then gradually begins to expand, not quite reaching its preevent size by the end of day 170.

[30] Figure 4 shows selected mappings of the ion differential energy flux in the magnetic equatorial plane between 0623 UT on day 169 and 0426 UT on day 170 (basically from the start of the main phase and into the recovery). The mappings are inversions of 8.6 keV centered images from the MENA NAI experiment. Inversions were produced using data averaged over five satellite spins to match the base EUV time resolution of 10 min. The individual plots use the same spatial layout as the He^+ density plots in Figure 2 (±6.0 R_E) even though the inversions are carried out to 8.0 R_E. Similar plots exist for each of the six HENA energy channels covering the energy range 10–81 keV. The ions follow the standard picture of the ring current within a storm: an ion injection from the tail, followed by earthward

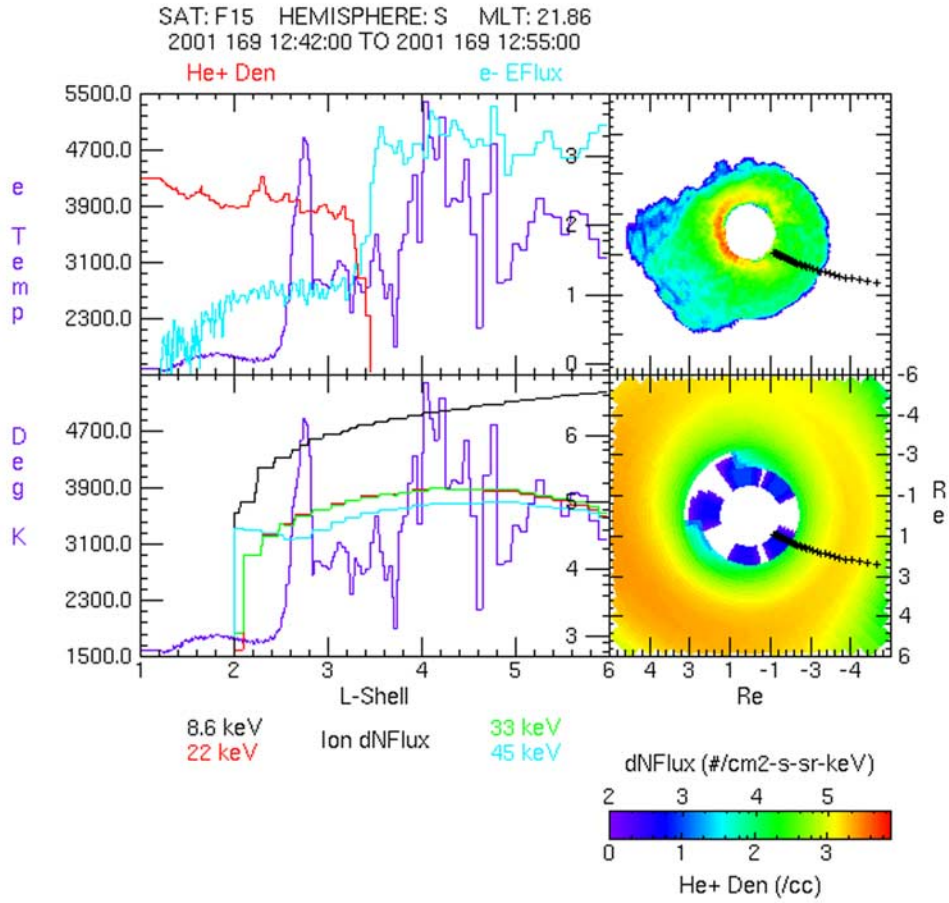

Figure 8. Relationship of the subauroral heating to the ring current ions. Upper two plots have identical format to those in Figures 6 and 7. Lower set of traces are the electron temperature (purple) together with the MENA 8.6 keV (black) and the HENA 13 (red), 22 (green), and 33 (cyan) keV ion fluxes along the satellite track. The fluxes are plotted in units of differential number flux (/cm^2 s sr keV) and are scaled according to the right-hand axis in the plot. Lower right-hand plot is the equatorial ion flux map generated from the HENA 22 keV centered neutral image with the satellite track overlaid. This is a borderline inner/outer event; offset from the plasmapause, narrow in extent, yet occurs within the full ring current energy spectrum. These types of events are commonly observed whenever the plasmapause is in close proximity to the equatorward edge of the auroral zone.

convection coupled with a gradient curvature drift to build the ring current and then eventual decay as the ion source turns off.

[31] Each DMSP spacecraft makes two cuts through the plasmaspheric latitudes every 101 min. These are either at 0928–2128 LT or 0545–1745 LT depending on the satellite. Figure 5 shows a southern hemisphere pass of the F12 DMSP satellite. It illustrates the more important storm time features observed in the auroral and subauroral ionosphere.

[32] Significant fluctuations in the ambient electron temperature are observed in the two crossings of the auroral oval (~1308–1311 UT and ~1321–1324 UT) and in the subauroral region (~1325–1326 UT). The heating within the auroral oval is a direct response to the observed electron precipitation and in higher time resolution plots the fluctuations in temperature are reasonably correlated with changes in the intensity of the electron precipitation. The subauroral heating, which in this case is seen only in the dusk sector, occurs outside of any major electron precipitation and more importantly without any accompanying ion precipitation. Ion precipitation is expected to accompany heating produced in the damping of ion cyclotron waves [*Cornwall et al.*, 1971]. In fact, in no instance in this entire storm is ion precipitation observed in conjunction with a subauroral temperature enhancement. It should be noted, however, that observations of ion precipitation attributed to EMIC waves are generally reported at higher altitudes than the DMSP satellites and often at energies above the upper cutoff of the SSJ/4 sensor [e.g., see *Yahnina et al.*, 2003; *Walt and Voss*, 2004]. There is a small density trough associated with the temperature enhancement in the figure. These are generally, but not always, seen in conjunction with duskside heating events.

[33] The location of the subauroral heating with respect to the plasmapause varies considerably over the time period studied. On the whole, we find that the events can be

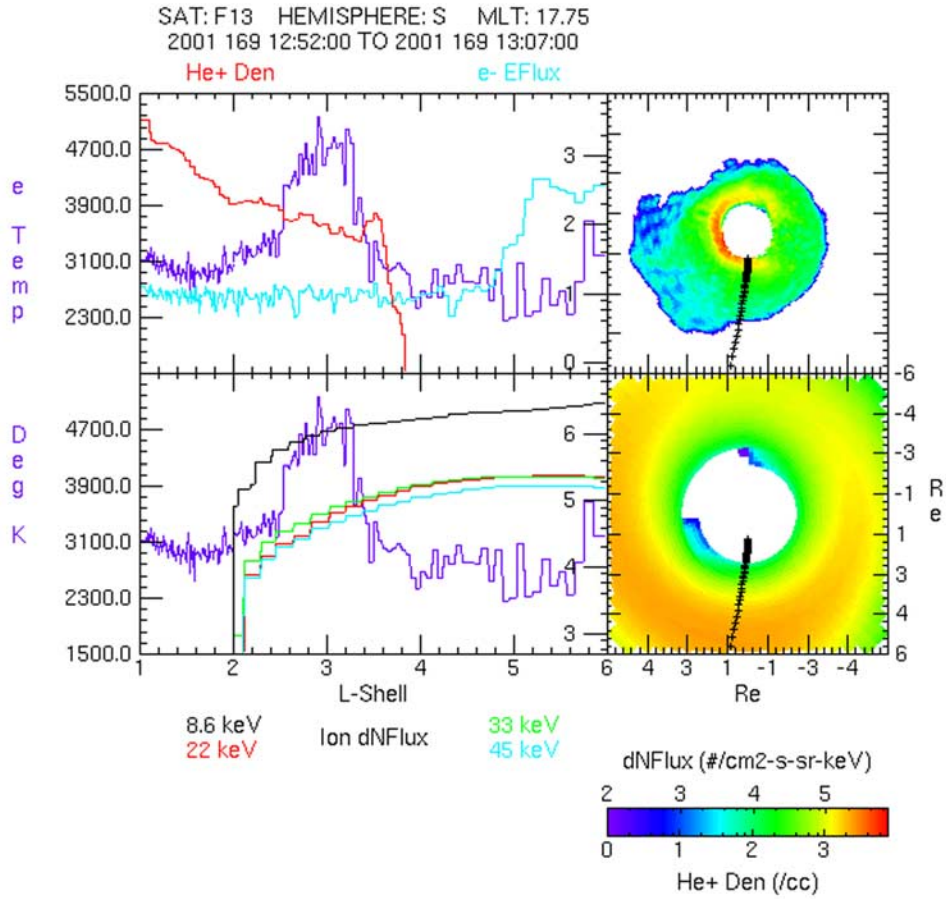

Figure 9. Identical in format to Figure 8 showing the subauroral heating in the dusk sector about 12 min after the event seen in Figure 8. Here the event is clearly an outer event; wide in extent and within the PBL. Other than the MLT there is little difference in the parameters seen in this event and that of Figure 8 with the exception of the separation of the plasmapause and the auroral zone.

divided into two classifications, which we call inner and outer events. Inner events occur >0.75 R_E earthward of the plasmapause and generally occur in the dawn sectors. Outer events occur within 0.75 R_E of the plasmapause (in the PBL) and are more prevalent in the evening sectors. These are the events which have been addressed by the numerous papers addressing the correlation between ionospheric heating and the plasmapause and SAR arcs. Examples of both event classifications are seen in Figures 6 and 7. The two figures show complete transequatorial DMSP crossings with subauroral heating in both hemispheres. A simple dipole mapping is used to project the satellite track onto the geomagnetic equatorial plane. Figure 6 is a dawn sector crossing, and Figure 7 a dusk sector crossing. The two subauroral heating events in each figure are separated by at most 30 min in time. The events in each figure are magnetically conjugate. It is extremely rare to find transequatorial crossings in which the heating is not magnetically conjugate. Conjugateness is evidence that the source of the heating lies in or near the geomagnetic equatorial plane and not in the ionosphere. Six sets of transequatorial plots can be assembled from the three DMSP spacecraft each orbit (101 min) allowing for excellent statistics.

[34] The trace of the electron flux (cyan) delineates the auroral and sub-auroral regions in each plot. The rapid rise in the electron flux is a good indicator that the satellite has crossed from the subauroral into the auroral zone. Enhancements in the electron temperature (blue) prior to this rise are subauroral heating events, while features after the rise are the result of auroral electron precipitation. The plasmapause is indicated by increased gradient in the He^+ density trace (red) at higher L.

[35] Figure 6 shows a pair of dawn sector heating events. These are inner events, well separated from the plasmapause and as with many dawn sector events, very narrow in extent and earthward of the PBL. Similar appearing events sometimes are seen when the plasmapause and the earthward auroral boundary coincide or nearly coincide (see Figure 8). These are generally set off from the plasmapause but within the PBL and classified as outer events.

[36] Compare Figure 6 with Figure 7, which shows a complex dusk sector crossing containing both an inner and outer heating event. It is uncommon to observe both types of events in a single sector. The complexity encountered in the figure is undoubtedly due to the fact that the satellite crosses through a bulge in the plasmasphere which extends to nearly 5 R_E in the premidnight sector. The outer heating event in this case actually seems to be formed by several individual events with the largest ($\sim L$ = 3.5) occurring at the approximate location of the inner plasmapause (deter-

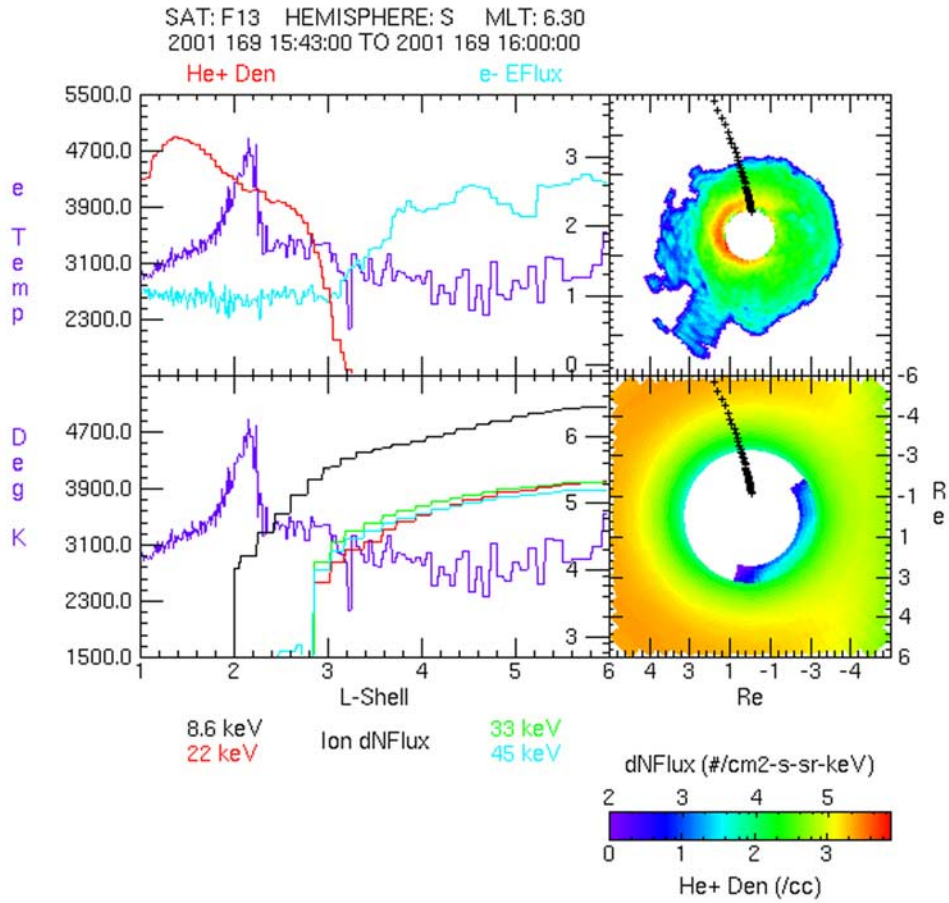

Figure 10. A typical dawnside inner heating event occurring during the recovery period. One of the primary characteristics of the inner heating events is that they are overlapped only by the lowest measured energy ring current ions.

mined by the location of the plasmapause on either side of the bulge) consistent with the findings of *Brace et al.* [1988]. The smaller peaks following the larger peaks occur within the bulge itself. In the upper crossing the smaller heating events actually extend beyond the boundary of the bulge. A close inspection of the original EUV image shows this not to be the case. In removing the large background in the images (refer to Figure 1) during the substorm, less sharp boundaries as occur in the vicinity of the bulge are sometimes artificially eroded causing the local edge of the plasmasphere to appear earthward of its actual location. The inner events in both Figures 6 and 7 appear to be correlated with a local enhancement in the plasmasphere density gradient.

[37] Figures 8 through 11 show the relationship of selected subauroral temperature enhancements to the equatorial ion flux. All show a deep penetration of the ring current into the plasmasphere. The cutoff of the MENA low-energy profile in the plots at $L = 2$ is an artifact of the inversion. To keep all of the inversions to the same range in L, the HENA inversions have been truncated below $L = 2$. These do occasionally show fluxes below $L = 2$ at the very lowest energies.

[38] Figure 8 is a midnight sector pass during the main phase of the storm. The heating is narrow in extent and separated from the plasmapause by about 0.5 R_E, a common occurrence when the equatorial edge of the auroral zone nearly coincides with the plasmapause as it does in this case. The ring current overlaps the temperature enhancement at all energies. The narrowness of the heating within the overlap region is a strong argument for an instability driven heat flux. Were a collisional induced heat flux the dominant transfer mechanism, the heating should be broadly observed throughout the overlap region.

[39] Figure 9 shows an F13 dusk sector pass which occurs about 10 min after the pass in Figure 8. Here, there is a broad subauroral temperature enhancement. The location of the earthward edge of the heating is almost identical in position to that in Figure 8. The outer edge, however, extends substantially farther outward, almost reaching the plasmapause. Other than the proximity of the equatorial edge of the auroral zone with the plasmapause in Figure 8 there appear to be no large differences between either the state of ring current or plasmasphere along the satellite track in Figures 8 and 9. Together the two figures give an indication of the longitudinal extent of the ionospheric heating, as well as how the heating profile will change with MLT.

[40] Figures 10 and 11 show a dawn and premidnight sector pass respectively during the storm's recovery phase. The passes are separated in time by about 25 min. By this time, the ion injection has stopped and the ring current

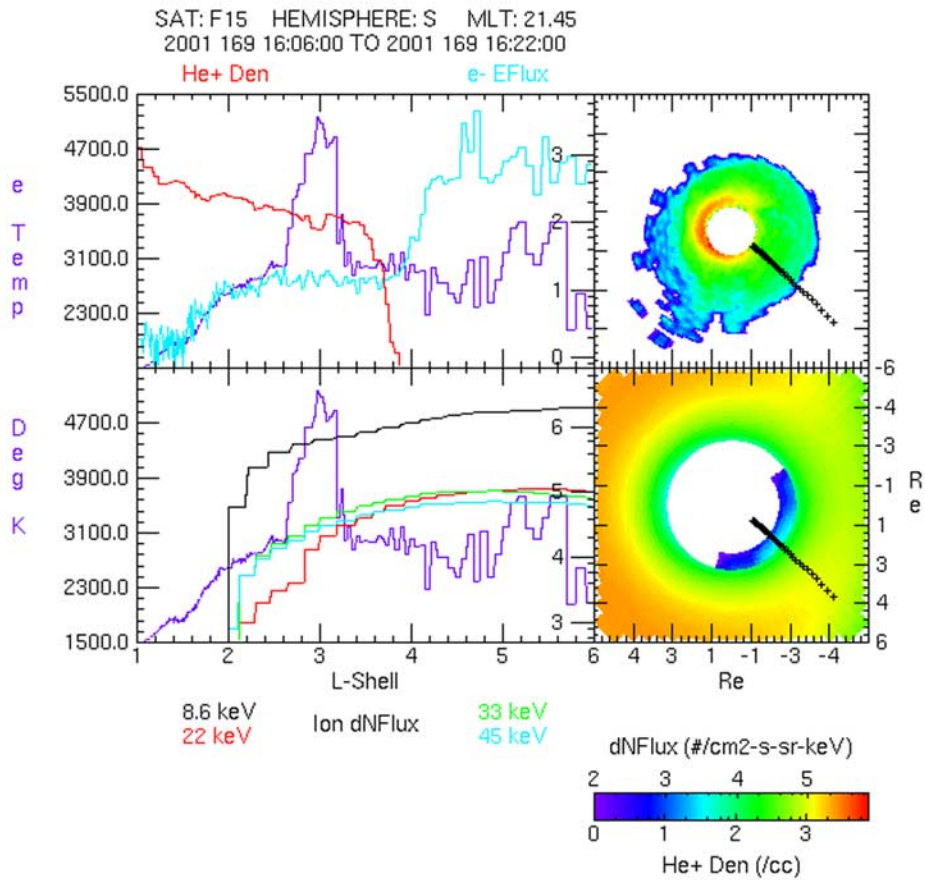

Figure 11. A nearly coincident observation of an outer heating event to that shown in Figure 10. The figure shows how the heating changes with MLT.

shows a distinctive minimum centered on the midnight sector. The two passes display the typical heating signatures expected for a dawn and premidnight crossing, inner heating in the dawn sector (Figure 10), and outer heating in the premidnight sector (Figure 11). What is striking in the two passes is the relationship of the ring current to the heating. As seen in Figure 11 (and Figures 8 and 9), heating in the dusk and premidnight sectors occurs in the presence of the full ring current energy spectrum. In the dawn and prenoon sectors, however, the heating occurs in the presence of the only the lower ring current energies which have a much deeper penetration. This is typical of inner events. This difference in energy coverage over the two events opens the question as to the importance of the ring current energy in the heat flux generation.

5. Discussion

[41] The variability in the magnetospheric plasma parameters under which the heating of the ambient topside electrons is observed to take place makes it difficult to point to a primary mechanism. Coulomb collisions occur throughout the plasmasphere/ring current overlap region. The amount of energy exchanged between the ring current and plasmasphere is proportional both to the number of scattering centers and to the energy and mass of the constituent ring current ions *Kozyra et al.* [1997]. If the mechanism responsible for the heat flux were Coulomb collisions alone, one would expect to observe a raised ionospheric temperature throughout the overlap region which is not observed. While the heating always is observed within the overlap region, it is for the most part localized in the radial direction (see Figures 8 or 11). This suggests that while the Coulomb collisions may be partly or wholly responsible for the heating of the equatorial plasmaspheric electrons, one or more alternate mechanisms act to transfer the heat into the upper ionosphere. These transfer mechanisms would act only under a restricted set of plasma conditions.

[42] Most instabilities satisfy this criteria. Instability growth rates are sensitive to the local plasma conditions (temperature anisotropy, hot to cold plasma density ratio, species, plasma beta, etc.) which will vary along radial cuts through the overlap region. The variations allow for the existence of restricted regions in which substantial growth rates for an individual instability can occur. Of the parameters noted above, the hot to cold ion density ratio is immediately available to us using the present data sets.

[43] The cold plasmasphere He^+ density is output directly from the inversion of the EUV images which can be extended to the H^+ plasmaspheric density through the use of various models [e.g., see *Craven et al.*, 1997]. To obtain the hot ion ring current density, it is necessary to first convert the differential number flux returned in the ion

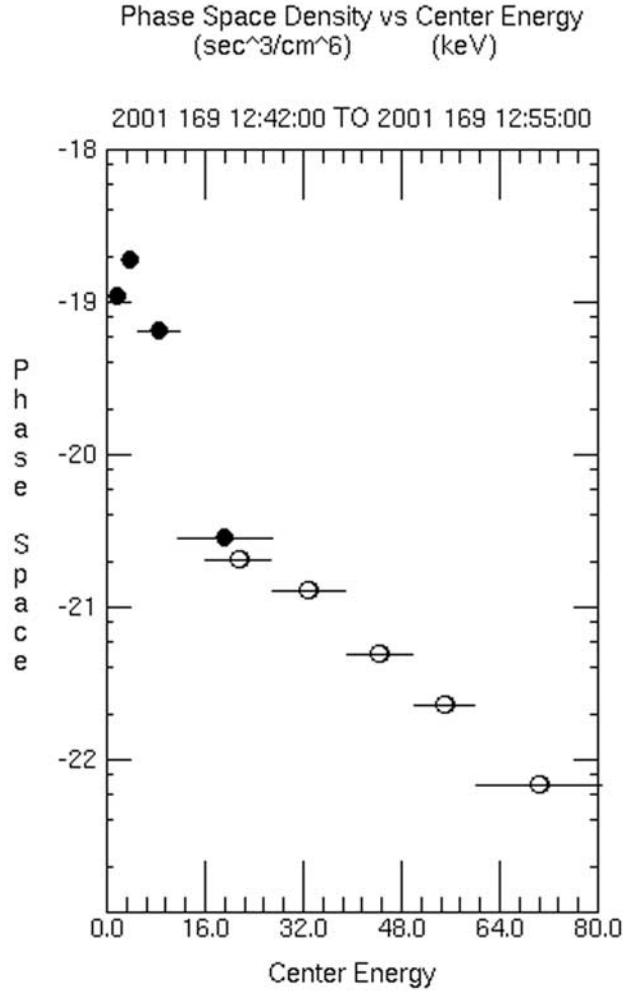

Figure 12. Typical ring current ion spectra derived from the HENA and MENA inversions. Solid circles are from MENA and open circles are from HENA. Horizontal lines indicate the width of the energy channels. Spectra shows dual Maxwellian signature.

inversions to units of velocity space distribution (s^3/cm^6) and then integrate over the distribution. Integrations are carried out by integrating over each energy bin under the assumption of isotropy and then summing the results. Figure 12 shows a typical ring current spectrum derived from the HENA and MENA inversions. The spectrum was measured about midway along the orbit track in Figure 8 and shows a two-component distribution which is not unusual in the ring current [*Kistler et al.*, 1989]. The actual integrations we performed to compute the density use only the 5–12 keV MENA channel and the upper five HENA channel data points. The HENA 10–16 keV energy channel (not shown on the plot) is not included in the integration nor is the MENA 11–27 keV channel which overlaps the HENA 16–27 keV channel.

[44] *Gomberoff and Neira* [1983] have shown that the EMIC instability growth rate is dependent not only on the ratio of hot to cold ions ratio but also on the ion species present. The dependence on the density ratio would lead to a naturally bounded region within the overlap region as the hot and cold ion densities vary inversely to one another as a function of *L*. Figures 13 through 17 plot the ratio of hot ring current to cold plasmasphere He^+ density (R_{HC}) as a function of the subauroral ionospheric temperature along the satellite track for several of the heating events in Figures 6 through 11. Data from different *L* shell intervals are plotted as different symbols which are annotated in the upper right of the figures. The gray background defines the upper limits of the plotted points and is included simply to make the features in the figures easier to discern.

[45] The figures indicate that enhanced ionospheric heating occurs within two restricted ranges of R_{HC}: 10^{-3}–10^{-2} and 10^{-5}–10^{-4}. The first (upper) range is associated with outer heating events and occurs primarily in the PBL while the second (lower) range correlates with inner heating events and occurs within the plasmasphere proper. Figure 17, which covers the time period in the upper set of plots in Figure 7, shows heating in both ranges corresponding to the inner and outer heating events observed in the pass. The occurrence of heating within confined R_{HC} bands is a strong argument for an instability as the driver of the heat flux into the ionosphere.

[46] The EMIC instability appears to be a likely candidate in driving the heat flux into the ionosphere as well as having some role in the generation of the equatorial heating of the plasmasphere [*Cornwall et al.*, 1971; *Khazanov et al.*, 2003]. General consensus is that the instability is probably active in the PBL when the ratio of hot to cold ion density is

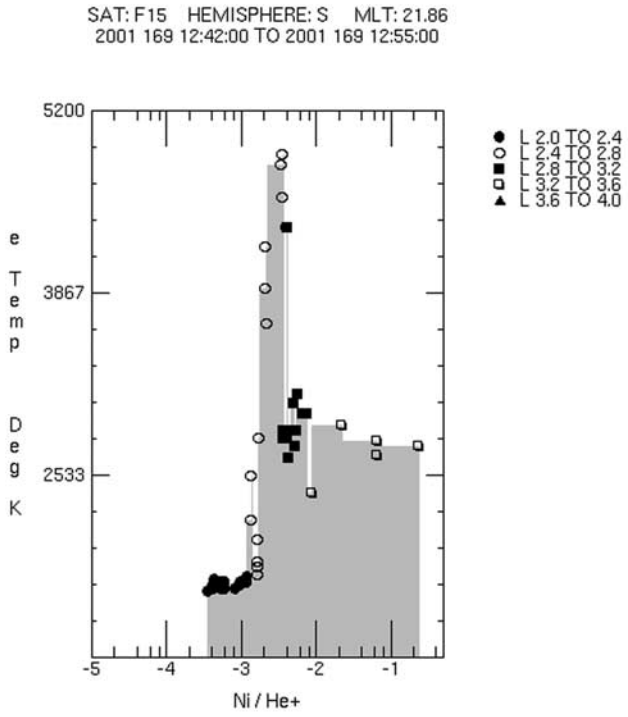

Figure 13. Topside electron temperature as a function of the hot to cold ion density ratio along the satellite track in Figure 8. Symbols indicate the *L* shell from which the ratios were obtained. The narrow peak centered at 3.5×10^{-3} shows that the heating occurs only with a narrow range of the density ratio.

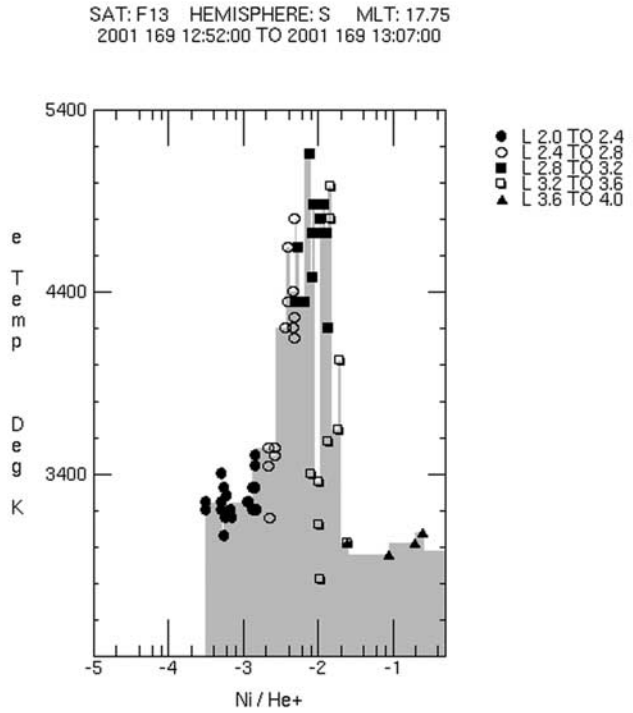

Figure 14. Identical to Figure 13 but covers the satellite track from Figure 9. This was a clear outer event and shows a similar restricted range to the heating as seen in Figure 13 which was classified as borderline inner/outer.

on the order of 0.01 [e.g., see *Cornwall et al.*, 1970; *Märk*, 1974]. Since the R_{HC} values in the figures only contain the He^+ density, is it necessary to include the H^+ contribution into the ratio before a comparison can be made between the predicted R_{HC} for strong EMIC growth and the range observed in which the heat flux is generated. To do this, we make use of the empirical relation for the ratio of He^+ to H^+ plasmaspheric ions given by *Craven et al.* [1997] and restated below:

$$\log_{10}\left(\frac{n_{He+}}{n_{H^+}}\right) = -1.541 - 0.176 \cdot R + 8.557 \times 10^{-3} \cdot P + 8.557 \times 10^{-5} \cdot P^2,$$

where R is the radial distance in R_E and P is a solar activity proxy which can be set to the daily $F_{10.7}$ value when $F_{10.7}$ is under 200. $F_{10.7}$ is ~200 for the entire time over which the storm occurs. Using this value with L 3.0 to 4.0 as an average range of the PBL gives a range of density ratios running from 0.11 to 0.07. The function is not rapidly varying over the interval, allowing us to use a simple mean value for the ratio of 0.09 which shifts the upper R_{HC} in the figures to 1.2×10^{-2} to 1.2×10^{-1}. This is exactly the range over which the EMIC instability is expected to be most active.

[47] It is not clear at this time what is driving the heat flux which occurs in the lower range of R_{HC}. As the plasmasphere density rises, the EMIC instability becomes collisionally damped [*Cornwall et al.*, 1970] and is not expected to be active within the R_{HC} range of the inner heating events. To our knowledge, very little if any work has been done addressing the source of these events. To fully understand what processes are generating this heat flux will probably require in situ measurements of the 3-D plasmasphere and ring current particle distributions from which candidate instabilities can be evaluated.

[48] While is appears that it is necessary that R_{HC} be within either the upper or lower range noted above for heat to be transferred into the ionosphere, this condition is not sufficient in itself to ensure that heating will occur. This is made clear in Figure 14 by the lack of heating in the upper R_{HC} range. Multiple conditions must be met before the instability becomes active of which R_{HC} is only one.

[49] There is enough evidence in the data to convincingly argue that the heat flux into the ionosphere associated with the topside heating events is instability-driven rather than the result of collisional heat conductance. It is also possible to show that data is consistent with an EMIC instability which is widely considered to be active in the PBL. The data, however, are not sufficient to uniquely identify a particular instability. This requires a more complete knowledge of the local plasma conditions than is currently available through the image inversions.

[50] In all of this we have neglected any role which the subauroral polarization stream (SAPS) might play in the heating. A detailed study of the correlation of SAPS and subauroral heating is beyond the scope of this paper; however, there are some general points which can be made. There is a recognized correlation between SAPS and elevated ionospheric electron temperatures [*Moffett et al.*, 1998; *Mishin and Burke*, 2005] but there has been no suggestion that SAPS provide either the driving force

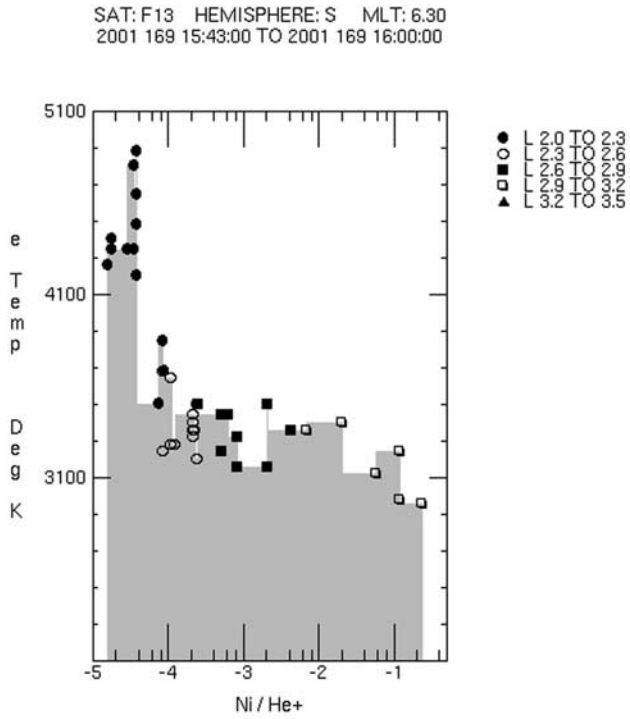

Figure 15. Identical to Figure 13 but covers the satellite track from Figure 10, an inner event. Inner events have their heating occurring at a much lower density ratio than outer events.

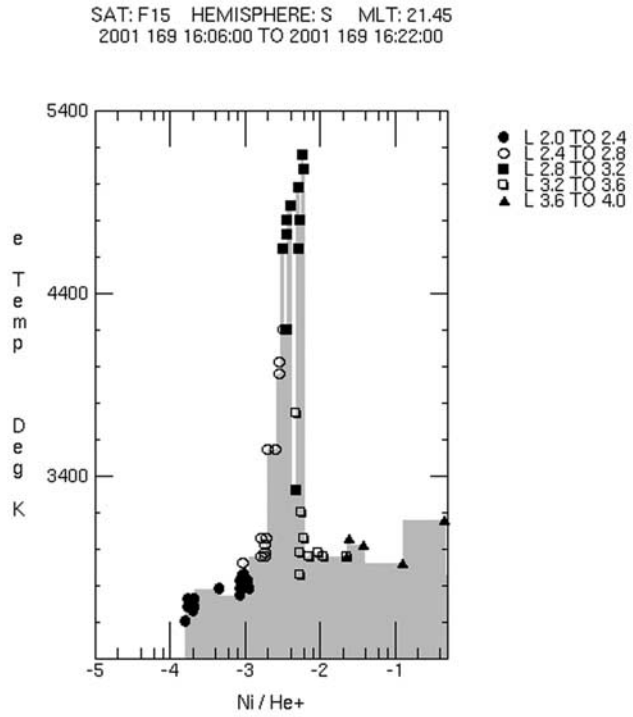

Figure 16. Identical to Figure 13 but covers the satellite track from Figure 11. Nearly coincident in time with plot in Figure 15 showing how the ratio changes for heating events at different MLT.

behind the heating or have a mitigating effect on it. The correlation itself is not surprising being that both are basically PBL phenomena.

[51] There are reasons to think that SAPS, if they do play a role in the enhancements in the subauroral heating, do not play a prominent one. Their variability both in intensity and spatial extent [*Foster and Vo*, 2002] does not seem to match the more constant thermal enhancements. Figures 18 and 19 show two subauroral thermal enhancements in the ambient electrons. In Figure 18 the heating (black trace in second plot) is seen to peak at about 0628 UT (1900 MLT) together with a increase in the measured sunward cross track drift ion velocity (red trace). The velocity is consistent with a local SAPS but is not proof that one exists. Figure 19 shows a similar heating event at about 1248 UT (2200 MLT) but in this event there is no direct correlation with an with a SAPS signature, although a SAPS signature is present poleward of the event between 1245:30 and 1246:45 UT. The presence of enhancements in the subauroral topside electron temperature outside of the region of ion drifts suggests that SAPS are probably not a direct driver of the heating. This does not rule out that it might modify the heating in some way, but it would be difficult to determine what effects it might have when coupled into the other variables involved (location, ionospheric density, etc.).

6. Conclusions

[52] We have presented examples showing the relationship of the topside heating of the subauroral ambient electrons with the plasmasphere and ring current for the 18–19 June 2001 magnetic storm. There are several interesting features observed in these events. These are summarized below with references back to the figures where appropriate.

[53] 1. Subauroral heating can be separated into two classifications: inner and outer heating events. Inner heating events occur well earthward of the plasmapause, while outer heating events occur in the vicinity of the plasmapause. Outer heating events are the events which have been generally addressed by previous authors (e.g., see Figure 7).

[54] 2. The heating occurs within the overlap region. The presence of both plasmasphere and ring current plasma on field lines where a heat flux is observed is a necessary condition (e.g., see Figures 8–11).

[55] 3. Inner heating events occur in the presence of only the lowest energy portion of the ring current spectra, while outer heating events occur in the presence of the full energy spectra (see Figure 10).

[56] 4. Heating events are observed only along portions of a radial cut through the overlap region and not along the entire cut. This implies that while Coulomb collisions may act as a heat source in the equatorial plasmasphere, collisional heat conduction is not the source of the heat flux into the ionosphere (e.g., see Figure 8).

[57] 5. The heat flux occurs within two ranges of R_{HC}. Outer heating events occur within the range in which EMIC waves are expected to have their maximum growth rate (e.g., see Figure 17).

[58] The overall picture of heat generation in the plasmasphere and the means by which it is transferred into the

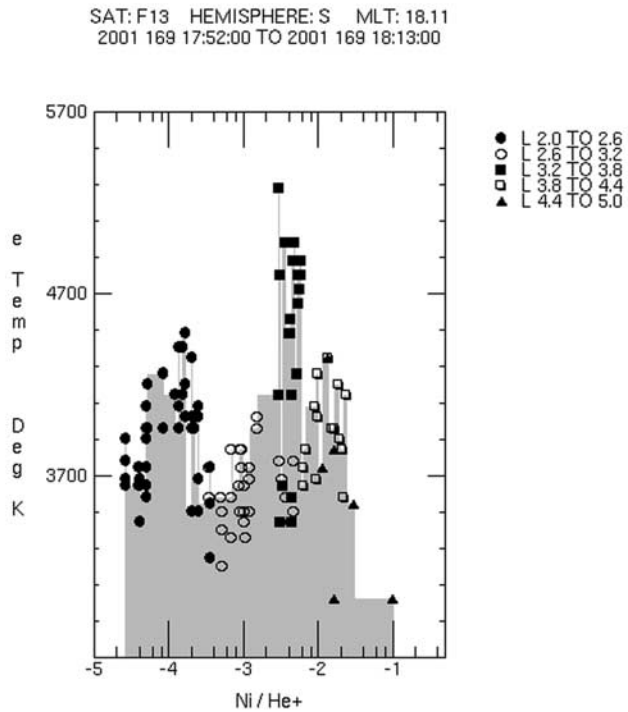

Figure 17. Identical to Figure 13 but covers the satellite track in the upper set of plots in Figure 7. The plots shows two distinct ratio intervals corresponding to the inner and outer events in Figure 7.

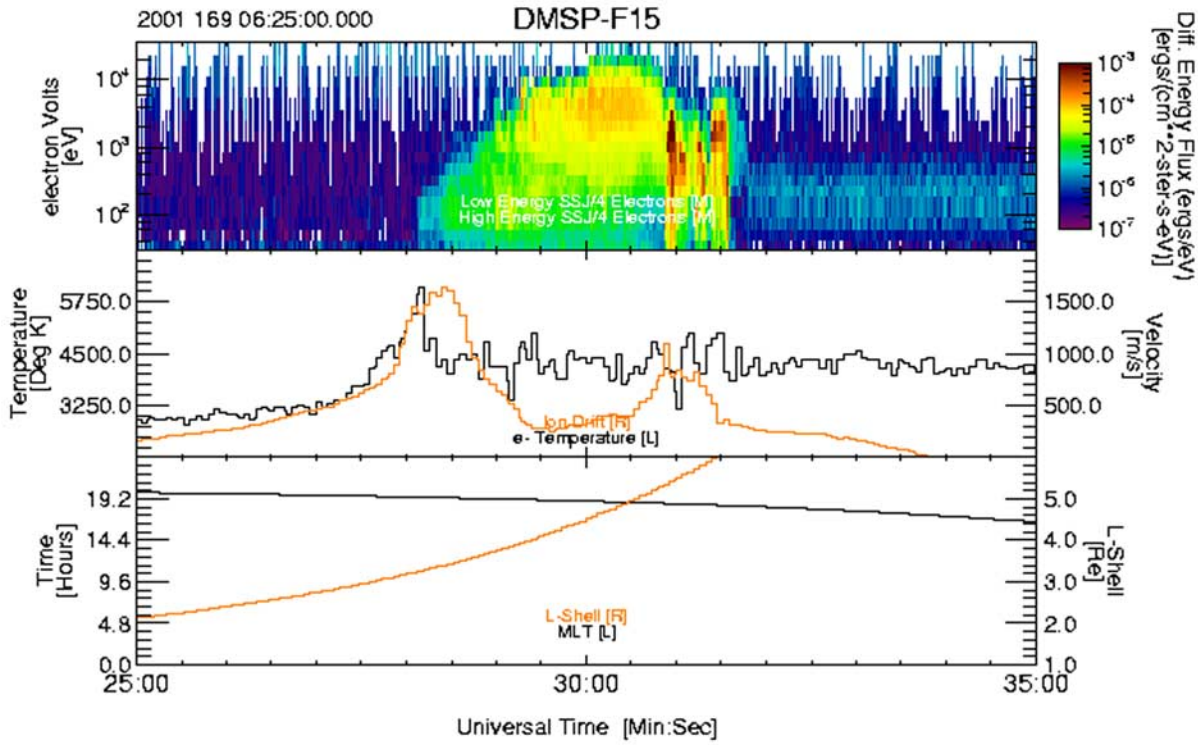

Figure 18. Plot of DMSP data showing a heating event at about 0628 UT from F15 occurring in conjunction with an increase in the cross track ion drift. Top spectrogram shows precipitating electrons and in units of differential energy flux. Line plots in the middle panel shows the ambient electron temperature (black) and the cross track ion drift velocity (orange). Lower set of line plots shows the satellite magnetic local time (black) and the L shell (orange).

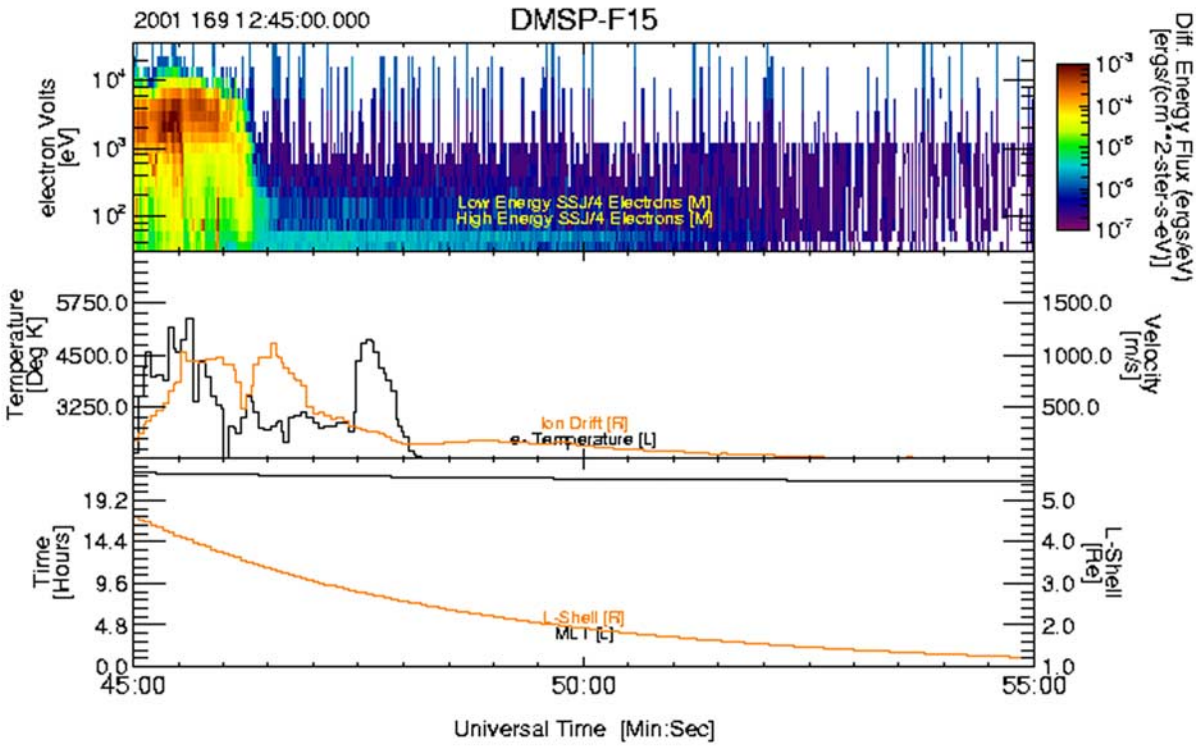

Figure 19. Plot similar to that shown in Figure 18, but in in this case the electron heating seen at 1248 UT does not occur in the presence of an ion drift.

upper ionosphere is not complete. Several outstanding questions remain. What is the heat flux driver for inner heating events? Is it instability-based as its association with a narrow range of R_{HC} would suggest, and if so, what is the relevant instability? Where are the precipitating ions which should accompany the EMIC instability in the outer heating events, or is EMIC, contrary to common belief, not the instability which is active? Finally, while we can use the equatorial R_{HC} to indicate globally where heating might occur within the ionosphere, we need to identify one or more parameters which will indicate where in these regions heating is occurring. This will probably require identification of the instabilities involved.

[59] **Acknowledgments.** The authors acknowledge support from subcontracts under NASA contract NAS5-96020 to Southwest Research Institute. The authors also gratefully acknowledge the Center for Space Sciences at the University of Texas at Dallas and the U.S. Air Force for providing the DMSP thermal plasma data as well as the Air Force Weather Agency which provides all of the DMSP data to the National Geophysical Data Center for long-term archive.

[60] Arthur Richmond thanks John Foster, George Khazanov, and Frederick J. Rich for their assistance in evaluating this paper.

References

Brace, L. H., R. C. Chappell, M. O. Chandler, R. H. Comfort, J. L. Horwitz, and W. R. Hoegy (1988), F region electron temperature signatures of the plasmapause based on Dynamics Explorer 1 and 2 measurements, *J. Geophys. Res.*, *93*, 1896.

Carpenter, D. L., and J. Lemaire (2004), The plasmasphere boundary layer, *Ann. Geophys.*, *22*, 4291.

Chandra, S. E., J. Maier, and P. Stubbe (1972), The upper atmosphere as regulator of subauroral red arcs, *Planet. Space Sci.*, *20*, 461.

Cole, K. D. (1965), Stable auroral red arcs, sinks for energy of Dst main phase, *J. Geophys. Res.*, *70*, 1689.

Cole, K. D. (1975), Coulomb collisions of ring current particles: Indirect source of heat for the ionosphere, *Tech. Rep. X-621-75-108*, NASA Goddard Space Flight Cent., Greenbelt, Md.

Cornwall, J. M., F. V. Coroniti, and R. M. Thorne (1970), Turbulent loss of ring current protons, *J. Geophys. Res.*, *75*, 4699.

Cornwall, J. M., F. V. Coroniti, and R. M. Thorne (1971), Unified theory of SAR arc formation at the plasmapause, *J. Geophys. Res.*, *76*, 4428.

Craven, P. D., D. L. Gallagher, and R. H. Comfort (1997), Relative concentration of He^+ in the inner magnetosphere as observed by the DE 1 retarding ion mass spectrometer, *J. Geophys. Res.*, *102*, 2279.

Erlandson, R. E., T. L. Aggson, W. R. Hogey, and J. A. Slavin (1993), Simultaneous observations of subauroral electron temperature enhancements and electromagnetic ion cyclotron waves, *Geophys. Res. Lett.*, *29*, 1723.

Fok, M. C., J. U. Kozrya, A. F. Nagy, and T. E. Cravens (1991), Lifetime of ring current particles due to coulomb collisions in the plasmasphere, *J. Geophys. Res.*, *96*, 7861.

Fok, M. C., J. U. Kozrya, A. F. Nagy, C. E. Rasmussen, and G. V. Khazanov (1993), Decay of equatorial ring current ions and associated aeronomical consequences, *J. Geophys. Res.*, *98*, 19,381.

Foster, J. C., and H. B. Vo (2002), Average characteristics and activity dependence of the subauroral polarization stream, *J. Geophys. Res.*, *107*(A12), 1475, doi:10.1029/2002JA009409.

Foster, J. C., M. J. Bounsato, M. Medillo, D. Nottingham, F. J. Rich, and W. Deng (1994), Coordinated stable auroral red arc observations: Relationship to plasma convection, *J. Geophys. Res.*, *99*, 11,429.

Gomberoff, L., and R. Neira (1983), Convective growth rate of ion cyclotron waves in a $H^+ - He^+$ and $H^+ - He^+ - O^+$ plasma, *J. Geophys. Res.*, *88*, 2170.

Gorbachev, O. A., G. V. Khazanov, K. V. Gamayunov, and E. N. Krivorutsky (1992), A theoretical model for the ring current interaction with the Earth's plasmasphere, *Planet. Space Sci.*, *40*, 859.

Green, J. L., J. J. H. Waite, R. C. Chappell, M. O. Chandler, J. R. Doupnik, P. G. Richards, R. Heelis, S. D. Shawhan, and L. H. Brace (1986), Observations of ionospheric magnetospheric coupling: DE and Chatanika, *J. Geophys. Res.*, *91*, 5803.

Hasagawa, A., and K. Mima (1978), Anomalous transport produced by kinetic Alfvén wave turbulence, *J. Geophys. Res.*, *83*, 1117.

Jordanova, V. K., R. M. Thorne, C. J. Farraugia, Y. Dotan, J. F. Fennell, M. F. Thompsen, G. D. Reeves, and D. J. McComas (2001), Ring current dynamics during the 13–18 July 2000 storm period, *Solar Phys.*, *204*, 361.

Khazanov, G. V., A. F. Nagy, T. I. Gambosi, M. A. Koen, and S. J. Cariglia (1992), Analytic description of the electron temperature behavior in the upper ionosphere and plasmasphere, *Geophys. Res. Lett.*, *19*, 1915.

Khazanov, G. V., T. I. Gambosi, O. A. Gorbachev, A. A. Trukhan, and R. H. Miller (1994), Thermodynamic effect of the ion sound instability in the ionosphere, *J. Geophys. Res.*, *99*, 5721.

Khazanov, G. V., K. V. Gamayunov, and V. K. Jordanova (2003), Self-consistent model of magnetopsheric ring current and electromagnetic waves: The 2–7 May 1998 storm, *J. Geophys. Res.*, *108*(A12), 1419, doi:10.1029/2003JA009856.

Kistler, L. M., F. M. Ipavich, D. C. Hamilton, G. Gloeckler, B. Wilken, G. Kremser, and W. Stüdemann (1989), Energy spectra of the major ion species in the ring current during geomagnetic storms, *J. Geophys. Res.*, *94*, 3579.

Kozyra, J. U., T. E. Cravens, A. F. Nagy, M. O. Chandler, L. H. Brace, B. A. Emery, and S. D. Shawhan (1982), Characteristics of a stable auroral red arc event, *Geophys. Res. Lett.*, *9*, 973.

Kozyra, J. U., E. G. Shelley, R. H. Comfort, L. H. Brace, T. E. Cravens, and A. F. Nagy (1987), The role of ring current O^+ in the formation of stable auroral red arcs, *J. Geophys. Res.*, *92*, 7487.

Kozyra, J. U., A. F. Nagy, and D. W. Slater (1997), High-altitudes energy source(s) for stable auroral red arcs, *Rev. Geophys.*, *35*, 155.

Lanzerotti, L. J., A. Hasagawa, and C. G. Maclennan (1978), Hydromagnetic waves as a cause of a SAR arc event, *Planet. Space Sci.*, *26*, 777.

Lundblad, J. Å., and F. Søraas (1978), Proton observations supporting the ion cyclotron wave heating theory of SAR arc formation, *Planet. Space Sci.*, *26*, 245.

Märk, E. (1974), Growth rates of the ion cyclotron instability in the magnetosphere, *Space Sci. Rev.*, *79*, 3218.

Mishin, E. V., and W. J. Burke (2005), Stormtime coupling of the ring current, plasmasphere, and topside ionosphere; Electromagnetic and plasma disturbances, *J. Geophys. Res.*, *110*, A07209, doi:10.1029/2005JA011021.

Mitchell, D. G., et al. (2000), High energy neutral atom (HENA) imager for the IMAGE mission, *Space Sci. Rev.*, *91*, 67.

Moffett, R. A., A. Ennis, G. Bailey, R. Heelis, and L. Brace (1998), Electron temperatures during rapid subauroral ion drift events, *Ann. Geophys.*, *16*, 450.

Norton, R. B., and J. A. Findley (1969), Electron temperature and density in the vicinity of the 29 September 1967 middle latitude red arc, *Planet. Space Sci.*, *17*, 1867.

Perez, J. D., M. C. Fok, and T. E. Moore (2000), Deconvolution of energetic neutral atom images of the Earth's magnetosphere, *Space Sci. Rev.*, *91*, 421.

Pollock, C. J., et al. (2000), Medium energy neutral atom (MENA) imager for the IMAGE mission, *Space Sci. Rev.*, *91*, 113.

Roelof, E. C., and A. J. Skinner (2000), Extraction of ion distributions from magnetospheric ENA and EUV images, *Space Sci. Rev.*, *91*, 437.

Sandel, B. R., et al. (2000), The extreme ultraviolet imager investigation for the IMAGE mission, *Space Sci. Rev.*, *91*, 197.

Thorne, R. M., and R. B. Horne (1997), Modulation of electromagnetic ion cyclotron instability due to interation with ring current, *Space Sci. Rev.*, *102*, 14,155.

Walt, M., and H. D. Voss (2004), Proton precipitation during magnetic substorms in August through November 1998, *J. Geophys. Res.*, *109*, A02201, doi:10.1029/2003JA010083.

Yahnina, T. A., et al. (2003), Low-frequency waves in the solar wind near Neptune, *Ann. Geophys.*, *21*, 2281.

C. Gurgiolo, Bitterroot Basic Research Inc., 837 Westside Road, Hamilton, MT 59840, USA. (chris@gurgiolo.com)

B. A. Larsen, Department of Physics, Space Science and Engineering Laboratory, P. O. Box 173840, Montana State University, Bozeman, MT 59717-3840, USA. (larsen@ssel.montana.edu)

D. G. Mitchell, Johns Hopkins University Applied Physics Laboratory, 11100 Johns Hopkins Road, Laurel, MD 20723, USA. (donald.g.mitchell@jhuapl.edu)

J. D. Perez, Physics Department, Auburn University, Auburn, AL 36849, USA. (perez@physics.auburn.edu)

C. J. Pollock, Southwest Research Institute, P. O. Drawer 28510, San Antonio, TX 78228-0510, USA. (cpollock@swri.edu)

B. R. Sandel, Lunar and Planetary Laboratory, University of Arizona, Sonett Space Sciences Building, 1541 East University Boulevard, Tucson, AZ 85721-0063, USA. (sandel@arizona.edu)